IEEE Access
Multidisciplinary | Rapid Review | Open Access Journal

Received 21 August 2022, accepted 16 November 2022, date of publication 21 November 2022,
date of current version 30 November 2022.

*Digital Object Identifier 10.1109/ACCESS.2022.3224020*

RESEARCH ARTICLE

# Analytical Modeling and Optimization of Partitioned Permanent Magnet Consequent Pole Switched Flux Machine With Flux Barrier

**WASIQ ULLAH, (Member, IEEE), FAISAL KHAN, (Senior Member, IEEE), SHAHID HUSSAIN, (Graduate Student Member, IEEE), MUHAMMAD YOUSAF, (Graduate Student Member, IEEE), AND SIDDIQUE AKBAR**

Electric Machine Design Research Laboratory, Department of Electrical and Computer Engineering, COMSATS University Islamabad, Abbottabad 22060, Pakistan

Corresponding author: Wasiq Ullah (wasiqullah014@gmail.com)

**ABSTRACT** Switched Flux Permanent Magnet Machine (SFPMM) encompass unique features of conventional direct current machine, permanent magnet (PM) synchronous machine and switch reluctance machine therefore, applicable for high-speed applications. However, conventional SFPMM exhibits demerits of high PM volume ($V_{PM}$), high torque ripples ($T_{rip}$), higher cogging torque ($T_{cog}$), lower torque density ($T_{den}$) and significant stator flux leakage. In this paper, a new topology of consequent pole (CP) SFPMM (CPSFPMM) is proposed having partitioned PM that improved flux modulation phenomena utilizing flux barriers. Moreover, due to non-linear behaviour of PM and complex stator structure alternate analytical sub-domain model is utilizes for initial design. However, initial design offers lower open-circuit phase flux linkage ($\Phi$), average mechanical torque ($T_{avg}$) and $T_{den}$. Aforementioned electromagnetic key performance indicator with $T_{cog}$, $T_{rip}$, total harmonics distortion in $\Phi$ ($\Phi_{THD}$), average power ($P_{avg}$) and power density ($P_{den}$) are refined utilizing Geometric-Based Deterministic Optimization (GBDO). Analysis reveals that proposed new topology of CPSFPMM with flux barriers reduces $T_{cog}$ by 34.90%, $T_{rip}$ by 20.27%, $\Phi_{THD}$ by 28.08% whereas it enhanced $P_{avg}$ by 17.79%, $T_{den}$ and $P_{den}$ by 34.38%.

**INDEX TERMS** Finite element analysis, analytical modeling, permanent magnet flux-switching machine, magnetic flux leakage, magnetic flux density distribution, permanent magnet machines, ac machines, brushless machines.

## I. INTRODUCTION

Switched Flux Machines (SFMs) are forms of stator-active brushless AC machines where all excitation sources, such as field winding, permanent magnets, and armature winding, are located on the stator, maintaining an inactive rotor constructed lamination sheets. SFMs are divided into three main groups based on the sources of their excitation: permanent magnet (PM) excited, field excited, and hybrid excited (PM and field excited). Dominant three topologies of the SFMs becomes Switched Flux Permanent Magnet Machines (SFPMM), Field Excited SFMs (FESFMs) and Hybrid Excited SFMs (HESFMs). Among these three SFMs topologies, SFPMM provides higher torque density therefore considered here for detail investigation regarding structure variations as well torque capability.

SFPMM constitute passive rotor (made of iron only) and stator encompassing Armature Winding (AW) slots and Permanent Magnet (PM). Alternate polarity PMs are sandwiched between AW slots where both PMs and AW are inserted in the stator. Due to the influence of centrifugal force and heat dissipation, such a design configuration prevents PM demagnetization. The passive rotor of SFPMM is developed from stack of steel lamination

The associate editor coordinating the review of this manuscript and approving it for publication was Christopher H. T. Lee.

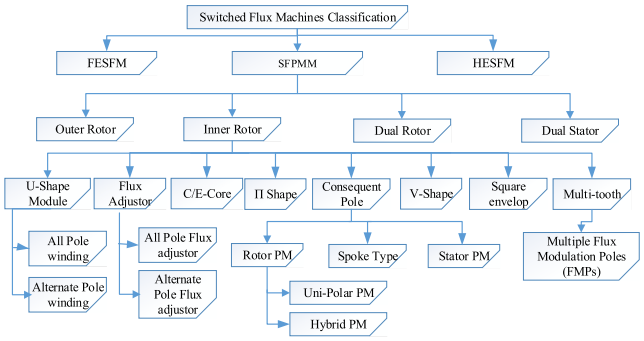


**FIGURE 1.** Detailed SFMs classification.

sheets. The back electromotive force (EMF) that results from SFPMM's double salient design resembles a sine wave and is consequently preferred for high-speed brushless applications.

SFPMMs are consider suitable candidate when high power density are primal requirements which make it applicable for domestic and industrial application such as electric vehicle traction [1], wind application [2], industrial servo and electric aircraft [3], electric bicycle and automotive industry [4]. However, SFPMM utilizes high PM volume which increase machines weight, cost and magnet eddy current losses [5]. Moreover, the PMs are extended to the stator yoke which causes serious issue of the flux leakages. In order to overcomes the aforesaid demerits of SFPMM are classified into various categories based on design topologies which are outer rotor, inner rotor, dual rotor and dual stator. With main concern in simple inner rotor topologies, PM-FSMs are further classified in U-shape Module, Flux adjustor, E/C-Core, $\pi$-shape, consequent pole, V-shape, square envelope, and multi-tooth as shown in Figure. 1. The above-mentioned SFMs categories reported in literature are results of overcoming the foregoing demerits of SFPMMs, however each design associates some drawbacks.

In order to suppress PM volume, reduce machine cost, diminish machine weight, and flux leakages, an overview is carried out in literature on different topologies of SFPMM [6], [7]. In [8] author proposed E-Core stator structure which reduces PM volume and increases AW slot area however, there is still significant leakages as shown in Figure. 2. The leakage flux is suppressed utilizing mechanical flux adjustor [9], [10] in all pole and alternate pole. Despite the significant utilisation of PM, this approach demands more mechanical peripherals, which unfavourably raises machine weight, volume, and cost.

Different topologies of SFPMM topologies such as $\pi$-form core of stator [11], multi-tooth stator core [12], V-type core [13] and square envelope [14] are recently delineate. However, despite of the high PM volume usage, $\pi$-shaped stator is complex in manufacturing and assembling, upper apex of modulation pole of multitooth may saturate due to narrow width, V-shape associate mechanical and electrical loading at the base of support between the V legs whereas

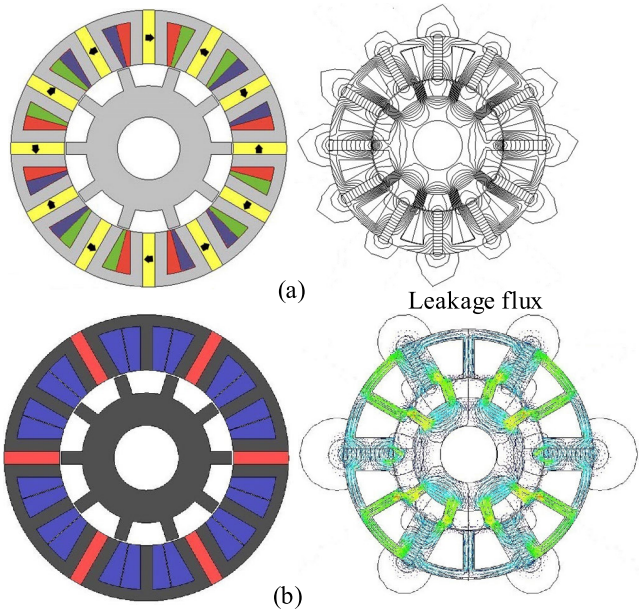


**FIGURE 2.** SFPMM with stator leakage flux (a) High PM usage SFPMM (b) Reduce PM E-Core SFPMM.

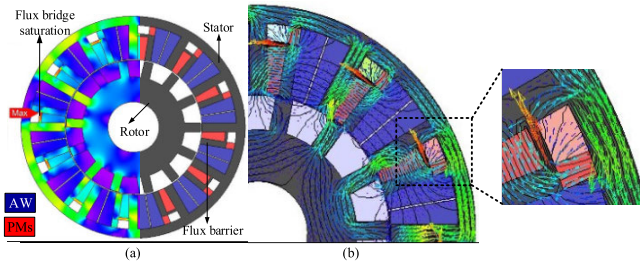


**FIGURE 3.** Conventional CPSFPMM (a) 2-D cross sectional view (b) Flux circulation and cancellation.

square envelop offer low torque density in compare with conventional SFPMM.

In order to suppress leakage flux recently various topologies of Consequent Pole (CP) machines are introduced. In [15], the author examines the existence of unipolar leakage flux with even order harmonics in CP rotor, while [16] CP and hybrid pole machines. Mechanical limitations aside, torque ripple and cogging torque effects predominate, leading to pulsing instantaneous torque. Using different magnetic poles, [17] suppresses torque ripple and cogging torque; nevertheless, in this approach, average torque drops. In order to preserve average torque, the author [18] adds spoke type rotor CP machines, but regrettably, core less density grows, and irreversible demagnetization occurs at the spoke sort PM corners closer to the air gap.

Author [19] effectively suppress the leakage flux by introducing Consequent Pole SFPMM (CPSFPMM) with flux bridges and flux barriers as illustrated in Figure. 3(a). This excellently supresses flux leakage of stator end however, PM utilization is high. Aside of high usage of magnet, the fine flux bridge saturates that worsen performance. Furthermore, flux bridges provide miniature track to the flux that

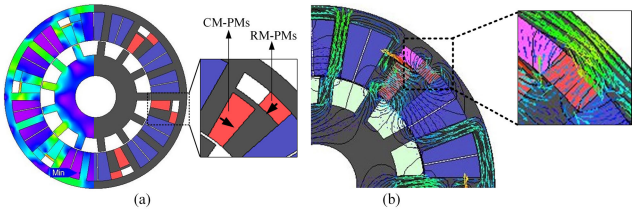


**FIGURE 4.** Proposed new topology of CPSFPMM (a) 2-D cross sectional view (b) Flux distribution at the flux bridge.

uplifting flux cancellation and circulation as indicated in Figure. 3(b) [20].

This research proposes a new CPSFPMM with reduced PM consumption, as illustrated in Figure. 4, to address the above-mentioned problems of increased PM consumption, flux leakages, magnet cost, machine weight, flux cancellation and circulation linked with SFPMM and CPSFPMM. Figure 4(a) tends to show clearly that CPSFPMM efficiently reduces the utilisation of the PMs by adding a poles alternative to PM and reducing flux cancellation and circulation. Additionally, Figure 4(b) demonstrates how CPSFPMM successfully lowers flux bridge saturation during initial design, when compared to the conventional current state of the art. Moreover, the new topology of the CPSFPMM offers lower torque ripple, cogging torque, and greater torque and power densities.

Numerical based Finite Element Analysis (FEA) method is intensively utilized for accurate modelling of electric machines and performance evaluation before proceeding to manufacturing and fabrication [21]. However, when used for initial sizing, and performance analysis, FEA incorporates geometric features, magnetic saturation, complicated stator structure, and non-linear behaviour of PMs, resulting in computational complexity and time-consuming [22]. Moreover, Finite Element (FE) analysis requires expensive software/hardware and large drive due to repeated iteration [23]. Therefore, author [20] suggest analytical model for initial design purpose.

To overcome computationally complexity, computational time, computer memory and drive storage this paper also utilizes alternate analytical sub-domain modelling approach in CPSFPMM for accurate prediction of magnetic field distribution in initial design phase machine sizing. The initial design obtained offer lower open-circuit phase flux linkage and low average mechanical torque therefore progressed to Geometric-Based Deterministic Optimization (GBDO) for enhancing aptitudes to attain improved performance and torque density. Analysis shows that as compared to the existing conventional model, the proposed novel CPSFPMM with less PM consumption demonstrates improved electromagnetic performance.

Main contributions in this paper is, author present CPSFPMM which successfully cuts 46.53% of PM usage. Moreover, analytical model (sub-domain approach) is investigated for preliminary sizing and validated by commercially available FEA package JMAG designer v18.1. Moreover,

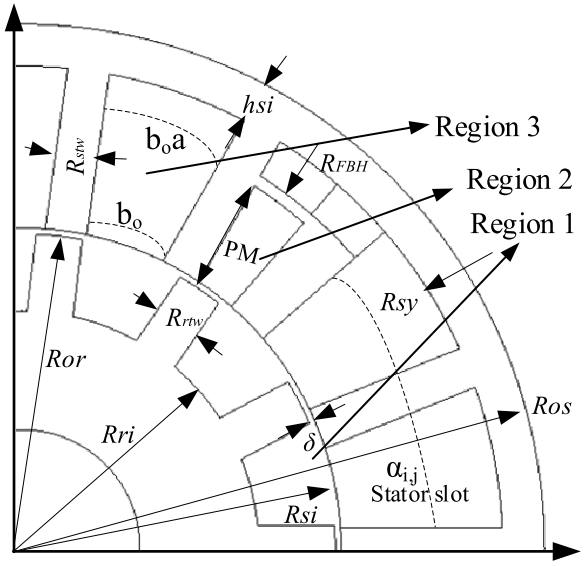


**FIGURE 5.** Design variables of CPSFPMM and sub-domain regions.

geometric-based deterministic optimization is carried out for enhancing capabilities of electromagnetic performance. Analysis reveals that the developed CPSFPMM at reduced PM usage offer 34.38% higher torque density and effectively curtailed inherent cogging torque and torque ripples by 34.9% and 20.27% respectively. Detailed performance analysis is listed in the proceeding sections.

In the following, section II extant to CPSFPMM construction, section III demonstrates formulation of analytical model. Section IV explains performance calculation, section V studied analytical model validation, section VI examines geometric-based deterministic optimization, section VII overview performance comparison. Finally, section VIII draws conclusions.

## II. CPSFPMM CONSTRUCTION

Figure. 4 shows that proposed CPSFPMM encompasses partitioned PM i.e., Radial Magnetized PMs (RM-PMs) and Circumferential Magnetized PMs (CM-PMs) in stator. The design variables are indicated in Figure. 5 and listed in Table 1. CPSFPMM model consist of E-core stator slot having alternate h-shaped stator tooth occupied by CM-PMs pole to reduce flux leakages going across the stator yoke and RM-PMs placed above h-shape stator tooth. Flux leakages from PM in poles are reduced with the help of the reverse magnetized radial PMs resulting in higher magnetic flux distribution in the stator yoke and hence improving the flux linkage by passing through alternative flux bridges and flux barriers and link to the rotor.

The proposed CPSFPMM improve magnetic field distribution where flux links directly through stator yoke with negligible reluctance. Hence magnetic field distribution and modulation effect in new topology of CPSFPMM is better compared to the existing conventional designs.

**TABLE 1. Design parameters of CPSFPMM.**

| Symbol | Unit | Value |
|---|---|---|
| $R_{os}$ | | 45 |
| $R_{sy}$ | | 41.4 |
| $R_{FBH}$ | | 37 |
| $h_{si}$ | | 3.6 |
| $R_{si}$ | mm | 27.5 |
| $R_{ri}$ | | 20.4 |
| $R_{or}$ | | 27 |
| $R_{rtw}$ | | 4 |
| $R_{stw}$ | | 4 |
| $\sigma$ | | 0.5 |

## III. FORMULATION OF ANALYTICAL MODEL

There are two phases in sub-domain model. As illustrated in Figure. 5, the whole field domain is first separated into subregions. The air gap, stator slots, and PMs are subregions of the field domains for proposed CPSFPMM. In this modeling, it is assumed that iron core is infinite permeable and end effect such as leakage flux is negligible.

By resolving the Poisson function enclosing the source in each subdomain, the general vector potential (GVP) formulation in subregions of the sub-domain is denoted by [24]

$$\frac{\partial^2 A_z}{\partial r^2}+\frac{1}{r}\frac{\partial A_z}{\partial r}+\frac{1}{r^2}\frac{\partial^2 A_z}{\partial \alpha^2} = \begin{cases} \left(\dfrac{\partial M_r}{\partial \alpha - M_\alpha}\right)\mu_o/r, & \text{in PMs} \\ 0, & \text{in air-gap} \\ -J\mu_o, & \text{in Stator slot} \end{cases} \tag{1}$$

whereas $r$ is the radius or circumference that varies with each boundary and interface conditions.

Sub-domain regions i.e., magnets, air gaps, and stator slots are examined independently for its general vector potential solution.

In the PM area, the GVP solution is stated as

$$A_{zII} = \left[\begin{array}{l} \displaystyle\sum_k \left(A_{IIk}\left(\frac{r}{R_{si}}\right)^k + B_{IIk}\left(\frac{r}{R_{ri}}\right)^{-k}\right)\cos(\alpha k) \\ \displaystyle+\sum_k \left(C_{IIk}\left(\frac{r}{R_{si}}\right)^k + D_{IIk}\left(\frac{r}{R_{ri}}\right)^{-k}\right)\sin(\alpha k) \end{array}\right] \tag{2}$$

Air-gap GVP solution is stated as

$$A_{zI} = \left[\begin{array}{l} \displaystyle\sum_k \left(A_{Ik}\left(\frac{r}{R_{ri}}\right)^k + B_{Ik}\left(\frac{r}{R_{ri}}\right)^{-k} + \frac{M_{ck\gamma}}{\mu_r\left(1-k^2\right)}\right) \\ \times \cos(\alpha k) \\ \displaystyle+\sum_k \left(C_{Ik}\left(\frac{r}{R_{ri}}\right)^k + D_{Ik}\left(\frac{r}{R_{ri}}\right)^{-k}\frac{M_{sk\gamma}}{\mu_r\left(1-k^2\right)}\right) \\ \times \sin(\alpha k) \end{array}\right] \tag{3}$$

Stator slot GVP solution is stated as

$$A_{zIII} = \mu_o J_{io}\left(R_{sy}^2 \ln\left(r-r^2\right)\right)\Big/2 + \left[\sum_k \left(\frac{J_{in}\mu_o}{F_n^2-4}r^2\right)\cos\left[\frac{\pi n}{d_{sa}}(\alpha-\alpha_i{+}0.5d_{sa})\right] + \sum_k \left(C_i\, R_{si}/R_{sy}\left(\frac{r}{R_{sy}}\right)^{\frac{\pi n}{d_{sa}}} + C_i\left(\frac{r}{R_{si}}\right)^{-\frac{\pi n}{d_{sa}}}\right)\cos\left[\frac{\pi n}{d_{sa}}(\alpha-\alpha_i{+}0.5d_{sa})\right]\right] \tag{4}$$

where $\mu_r$ is relative permeability, $k$ is harmonics order, $J$ is current density, $A_{Ik}, B_{Ik}, C_{Ik}, D_{Ik}, A_{IIk}, B_{IIk}, C_{IIk}$, and $D_{IIk}$ are Fourier coefficient.

The foremost source in CPSFPMM is AW and partitioned PMs. Magnetization of magnet distribution are stated as summation of cosine and sine harmonics as [25]

$$M = M_r r + M_\theta \alpha \tag{5}$$

$$M_r = \sum_{k=1,3,4}\left(M_{rck}\cos(\alpha k) + M_{rsk}\sin(\alpha k)\right) \tag{6}$$

$$M_\theta = \sum_{k=1,3,4}\left(M_{\theta ck}\cos(\alpha k) + M_{\alpha sk}\sin(\alpha k)\right) \tag{7}$$

whereas $M_\theta$ and $M_r$ is tangential and radial magnetization components.

$$M_{rck} = M_{rk}\cos(\omega_r k t + \alpha_o k) \tag{8}$$

$$M_{rsk} = M_{rk}\sin(\omega_r k t + \alpha_o k) \tag{9}$$

$$M_{\theta ck} = -M_{\theta k}\sin(\omega_r k t + \alpha_o k) \tag{10}$$

$$M_{\theta sk} = M_{\theta k}\cos(\omega_r k t + \alpha_o k) \tag{11}$$

where $M_{\theta sk}$ and $M_{\theta ck}$ are magnitude of $k_{th}$ order sine and cosine tangential magnetization, $M_{rsk}$ and $M_{rck}$ are magnitude of $k_{th}$ order sine and cosine radial magnetization patterns and $\omega_r$ is rotor rotational speed.

Additionally, the current density for non-overlap winding design in the $i_{th}$ armature winding slot may be given as [25].

$$J = 0.5\left(J_{i1}+J_{i2}\right) + \sum J_{in}\cos\left[\frac{n\pi}{d_{sa}}(\alpha+0.5d_{sa}-\alpha_i)\right] \tag{12}$$

$$J_{in} = 2/\pi n\left(J_{i1}-J_{i2}\right)\sin(0.5\pi n) \tag{13}$$

Typically, the magnetic flux density (MFD) tangential and radial components are given by [27]

$$B_r = \left(\frac{1}{r}\right)\frac{\partial A_z}{\partial \alpha} \tag{14}$$

$$B_\theta = -\frac{\partial A_z}{\partial r} \tag{15}$$

Air-gap MFD components are stated as

$$B_{Ir} = \frac{1}{r}\sum_k -k\left[A_{Ik}\left(\frac{r}{R_{si}}\right)^k + B_{Ik}\left(\frac{r}{R_{ri}}\right)^{-k}\right]\sin(k\alpha) + \frac{1}{r}\sum_k k\left[C_{Ik}\left(\frac{r}{R_{si}}\right)^k + D_{Ik}\left(\frac{r}{R_{ri}}\right)^{-k}\right]\cos(k\alpha) \tag{16}$$

$$B_{I\theta} = -\sum_k -k\left[\frac{A_{Ik}}{R_s}\left(\frac{r}{R_{si}}\right)^{k-1} + \frac{B_{Ik}}{R_{ri}}\left(\frac{r}{R_{ri}}\right)^{-k-1}\right] \times \cos(k\alpha) - \sum_k k\left[\frac{C_{Ik}}{R_{si}}\left(\frac{r}{R_{si}}\right)^{k-1} + \frac{D_{Ik}}{R_{ri}}\left(\frac{r}{R_{ri}}\right)^{-k-1}\right]\sin(k\alpha) \quad (17)$$

PMs MFD components are stated as

$$B_{IIr} = \frac{1}{r}\sum_k -k\left[A_{IIk}\left(\frac{r}{R_{ri}}\right)^{k} + B_{IIk}\left(\frac{r}{R_{ri}}\right)^{-k} + \frac{\mu_o M_{ck} r}{(k^2-1)}\right] \times \sin(k\alpha) + \frac{1}{r}\sum_k k\left[C_{IIk}\left(\frac{r}{R_{ri}}\right)^{k} + D_{IIk}\left(\frac{r}{R_{ri}}\right)^{-k} + \frac{\mu_o M_{sk} r}{(k^2-1)}\right]\cos(k\alpha) \quad (18)$$

$$B_{II\theta} = \sum_k \left[\frac{A_{IIk}}{R_{si}}\left(\frac{r}{R_{ri}}\right)^{k-1} - \frac{B_{IIk}}{R_{ri}}\left(\frac{r}{R_{ri}}\right)^{-k-1} + \frac{\mu_o M_{ck}}{(k^2-1)}\right] \times \cos(k\alpha) + \sum_k \left[\frac{C_{IIk}}{R_{ri}}\left(\frac{r}{R_{ri}}\right)^{k-1} - \frac{D_{IIk}}{R_{ri}}\left(\frac{r}{R_{ri}}\right)^{-k-1} + \frac{\mu_o M_{sk}}{(k^2-1)}\right]\sin(k\alpha) \quad (19)$$

Armature slots MFD components i.e., radial and tangential are expressed as

$$B_{IIIr} = -\sum_k \left\{\left[\frac{n\pi}{d_{sa}} C_i\left(\left(\frac{R_{si}}{R_{sy}}\right)^{\frac{n\pi}{d_{sa}}} + \left(\frac{r}{R_{si}}\right)^{-\frac{n\pi}{d_{sa}}}\right)\right]\Big/ r + J_{in}\mu_o\left[\frac{n\pi}{d_{sa}} r - 2R_{sy}\left(\frac{r}{R_{sy}}\right)^{\frac{n\pi}{d_{sa}}-1}\right]\Big/\left(\frac{n\pi}{d_{sa}}^2 - 4\right)\right\} \times \sin\left[\frac{n\pi}{d_{sa}}(\alpha - \alpha_i + 0.5 d_{sa})\right] \quad (20)$$

$$B_{III\theta} = -0.5 J_{io}\mu_o\left(R_{sy}^2 - r^2\right)\Big/ r - \sum_k \left\{\left[\frac{n\pi}{d_{sa}} C_i\left(\left(\frac{R_{si}}{R_{sy}}\right)^{\frac{n\pi}{d_{sa}}} - \left(\frac{r}{R_{si}}\right)^{-\frac{n\pi}{d_{sa}}}\right)\right]\Big/ r + 2J_{in}\mu_o\left[r - 2R_{sy}\left(\frac{r}{R_{sy}}\right)^{\frac{n\pi}{d_{sa}}-1}\right]\Big/\left(\frac{n\pi}{d_{sa}}^2 - 4\right)\right\} \times \cos\left[\frac{n\pi}{d_{sa}}(\alpha - \alpha_i + 0.5 d_{sa})\right] \quad (21)$$

Boundary and interface conditions are employed to compute unknown Fourier coefficients

$$B_{I\theta}|_{r=R_{or+\sigma/2}} = B_{II\theta}|_{r=R_{si}}\alpha_i + \frac{f}{2} < \alpha < \alpha_i - \frac{f}{2} \quad (22)$$

$$B_{I\theta}|_{r=R_{or+\sigma/2}} = B_{II\theta}|_{r=R_{si}}\alpha_j + \frac{g}{2} < \alpha < \alpha_j - \frac{g}{2} \quad (23)$$

where the stator tooth opening angle is $g$ and the slot opening angle is $f$. The left and right sides of the interface conditions are translated to the equivalent interim for magnetic flux density constituent since they take the form of a Fourier series of various intervals. Over the interval $[-\pi, \pi]$ the left half of the formula transforms into a Fourier series, and the right side of the Fourier series is

$$\left[\alpha_i - \frac{f}{2}, \alpha_i + \frac{f}{2}\right] \text{ or } \left[\alpha_j - \frac{f}{2}, \alpha_j + \frac{f}{2}\right] \quad (24)$$

Using a piecewise function and extending Fourier series in the $[-\pi, \pi]$ range, the GVP over boundary condition is represented as

$$A_{I\theta}|_{r=R_{or+\sigma/2}} = A_{II\theta}|_{r=R_{si}}\alpha_i + \frac{f}{2} < \alpha < \alpha_i - \frac{f}{2} \quad (25)$$

$$A_{I\theta}|_{r=R_{or+\sigma/2}} = A_{II\theta}|_{r=R_{si}}\alpha_j + \frac{g}{2} < \alpha < \alpha_j - \frac{g}{2} \quad (26)$$

The left side transformed to Fourier series over interim to make applying the boundary and interface condition

$$\left[\alpha_i - \frac{f}{2}, \alpha_i + \frac{f}{2}\right] \text{ or } \left[\alpha_j - \frac{g}{2}, \alpha_j + \frac{g}{2}\right] \quad (27)$$

Fourier coefficient equation can be used as follows

$$C_i\left(\frac{R_{si}}{R_{si}}\right)^{m\pi/f} + D_i = \sum_k \left[\left(A_{IIk} + B_{IIk}\left(\frac{R_{ri}}{R_{si}}\right)^{k}\right)\frac{2\pi\eta_{si}}{f} + \left(C_{IIk} + D_{IIk}\left(\frac{R_{ri}}{R_{si}}\right)^{k}\right)\frac{2\pi\varepsilon_{si}}{g}\right] \quad (28)$$

$$C_j\left(\left(\frac{R_{si}}{R_{FBH}}\right)^{2\frac{l\pi}{g}} + 1\right) = \sum \left[\left(A_{IIk} + B_{IIk}\left(\frac{R_{ri}}{R_{si}}\right)^{k}\right)\frac{2\pi\eta_{si}}{f} + \left(C_{IIk} + D_{IIk}\left(\frac{R_{ri}}{R_{si}}\right)^{k}\right)\frac{2\pi\varepsilon_{si}}{g}\right] \quad (29)$$

In the following boundary condition, the tangential magnetic field contribution is zero at the yoke of rotor.

$$B_{I\theta}|_{r=h_{si}} = -\frac{1}{\mu_r}M_\theta = 0 \quad (30)$$

Applying condition $M_\theta = 0$, The radial magnetization component is stated as

$$\sum_k \left[\frac{A_{Ik}}{R_{ri}}\left(\frac{R_{ri}}{R_{ri}}\right)^{k-1} - \frac{B_{Ik}}{R_{ri}}\left(\frac{R_{ri}}{R_{si}}\right)^{-k-1} + \frac{\mu_o M_{ck}}{(k^2\text{-}1)}\right] \times \cos(k\alpha) + \sum_k \left[\frac{C_{Ik}}{R_{ri}}\left(\frac{R_{ri}}{R_{ri}}\right)^{k-1} - \frac{D_{Ik}}{R_{ri}}\left(\frac{R_{ri}}{R_{si}}\right)^{-k-1} + \frac{\mu_o M_{sk}}{(k^2\text{-}1)}\right]\sin(k\alpha) = 0 \quad (31)$$

$$\frac{A_{Ik}}{R_{ri}}\left(\frac{R_{ri}}{R_{ri}}\right)^{k-1} - \frac{B_{Ik}}{R_{ri}}\left(\frac{R_{ri}}{R_{si}}\right)^{-k-1} + \frac{\mu_o M_{ck}}{(k^2-1)} = 0 \quad (32)$$

$$\frac{C_{Ik}}{R_{ri}}\left(\frac{R_{ri}}{R_{ri}}\right)^{k-1} - \frac{D_{Ik}}{R_{ri}}\left(\frac{R_{ri}}{R_{si}}\right)^{-k-1} + \frac{\mu_o M_{sk}}{(k^2-1)} = 0 \quad (33)$$

Simplifying $B_{Ik}$ and $D_{Ik}$ in term of $A_{Ik}$ and $C_{Ik}$ as

$$B_{Ik} = \frac{A_{Ik}\left(\frac{R_{ri}}{R_{si}}\right)^{k} + \mu_o R_{ri}(kM_{\theta ck} - M_{rsk})}{(k^2-1)} \quad (34)$$

$$D_{Ik} = \frac{C_{Ik}\left(\frac{R_{ri}}{R_{si}}\right)^{k} + \mu_o R_{ri}(kM_{\theta ck} + M_{rsk})}{(k^2-1)} \quad (35)$$

The Fourier coefficients $A_{Ik}$, $B_{Ik}$, $C_{Ik}$, $D_{Ik}$, $A_{IIk}$, $B_{IIk}$, $C_{IIk}$ and $D_{IIk}$ is computed utilizing first order multi-variable equations [24], [25], [26], [27] whereas detailed formulation of the sub-domain model can found in [30].

## IV. PERFORMANCE CALCULATION

Performance of the proposed CPSFPMM is calculated under no-load and loaded condition.

The flux linkage related to the AW coils set of the phase makes up the open-circuit phase flux linkage for that phase. Open-circuit phase flux linkage is computed using vector potential distribution [27]

$$\Phi = \frac{LN}{A}\int_{R_{si}}^{R_{sy}}\int_{\alpha_1}^{\alpha_2} A_z r dr d\alpha \quad (36)$$

$$\Phi = \frac{LN}{A}\int_{R_{si}}^{R_{sy}}\int_{\alpha_1}^{\alpha_2+0.5d_{sa}} A_z r dr d\alpha \quad (37)$$

Additionally, the no-load torque that a machine exhibits as a result of the attraction of the PMs and AW slots is known as cogging torque. Cogging torque produces acoustic noise and vibration, which is undesirable in applications, particularly in robots. The Maxwell Stress Tensor (MST) approach described in [3] with cosine and sine component of tangential and radial MFD is useful for computation of the cogging torque CPSFPMM

$$T_{cog} = \frac{r^2 L}{\mu_o}\int_0^{2\pi} B_{Ir}B_{I\theta}d\theta = \frac{\pi r^2 L}{\mu_o}\sum_k B_{rck}B_{\theta ck} + B_{rsk}B_{\theta sk} \quad (38)$$

where $B_{rck}$ is radial cosine, $B_{\theta ck}$ is tangential cosine, $B_{rsk}$is radial sine, and $B_{\theta sk}$ is tangential sine components of MFD.

Finally, the torque produced under loaded condition is referred as mechanical torque. Using tangential and radial components of MFD and the Maxwell Stress Tensor (MST) approach described in [1], mechanical torque of CPSFPMM is calculated

$$T = \frac{r^2 L}{\mu_o}\int_0^{2\pi} B_{Ir}B_{I\theta}d\theta \quad (39)$$

where $B_{Ir}$ and $B_{I\theta}$ are radial and tangential component of MFD, respectively.

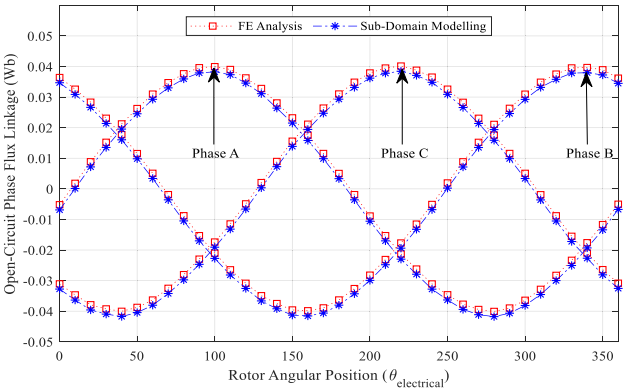


**FIGURE 6.** Predicted FE analysis and analytical open circuit flux linkage.

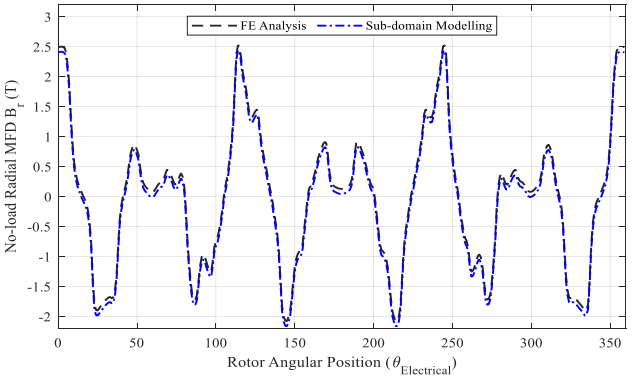


**FIGURE 7.** Predicted FE analysis and analytical of no-load radial MFD component.

## V. ANALYTICAL MODEL VALIDATION

Based on the parameters mentioned in table 1, the sub-domain analytical model is validated using JMAG FEA package. To accurately determine the electromagnetic performance of the CPSFPMM, transient analysis is performed at a speed of 1200 $r/min$ and a current density of 15 $A/mm^2$.

In order to validate analytical sub-domain model some of the key assumptions, boundary conditions and excitation are (*i*) Rotor and stator are assigned material considering infinite permeability, (*ii*) Magnetization direction of the PMs are radial and circumferential alignment, (*iii*) Position of rotor tooth with stator are in aligned position, (*iv*) All PMs segments have same magnetic properties and dimensions, (*v*) Developed CPSFPMM is rotary in nature with periodic air-gap permeances, therefore only one pole pitch periodic boundary is considered and (*vi*) 15 $A/mm^2$ excitation current density is applied to the armature winding. Furthermore, it is worth mentioning that both in sub-Domain Modelling and FEA validation, magnetic saturation is not considered yet therefore, the peak values of magnetic flux densities reach to 3.75T in on load radial component.

Under no-load condition, Figure. 6 contrasts the open-circuit phase flux linkage results from the related FE analysis and analytical sub-domain results. Open-circuit phase

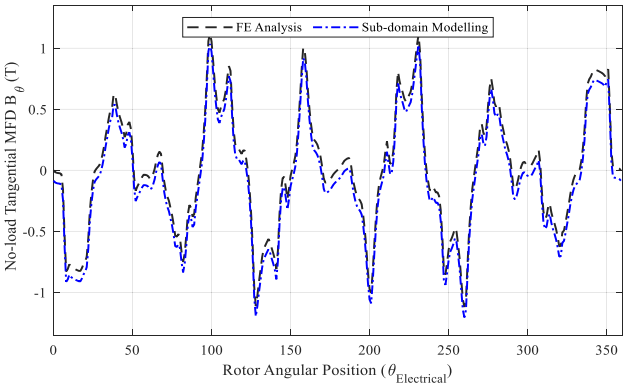


**FIGURE 8.** Predicted FE analysis and analytical sub-domain of no-load tangential MFD component.

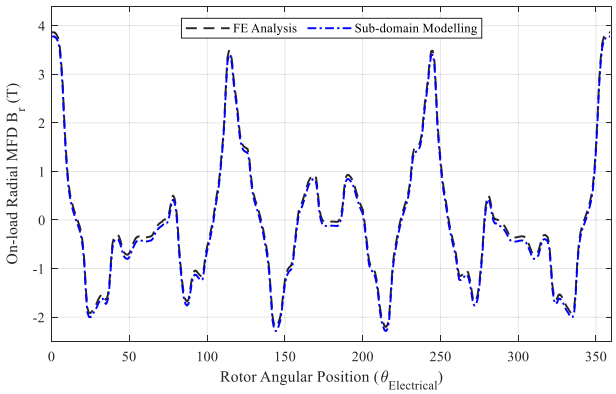


**FIGURE 9.** Predicted FE analysis and analytical sub-domain of on-load radial MFD component.

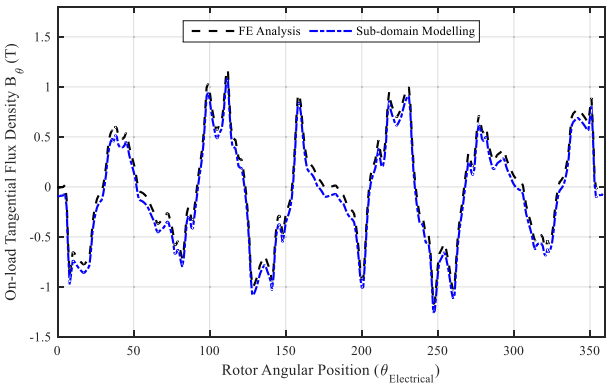


**FIGURE 10.** Predicted FE analysis and analytical sub-domain of on-load tangential MFD component.

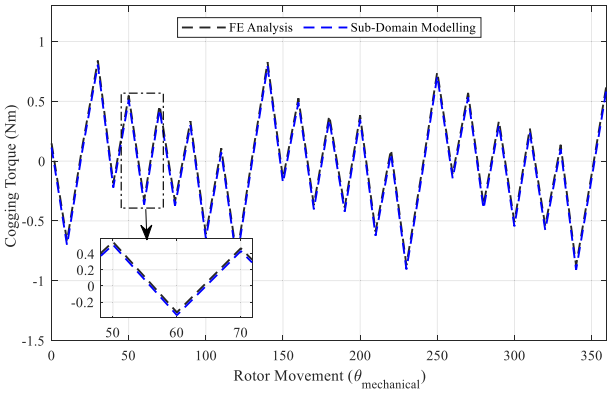


**FIGURE 11.** FE analysis and analytical sub-domain prediction of cogging torque.

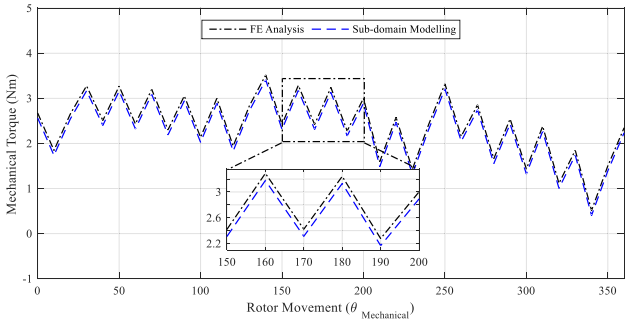


**FIGURE 12.** FE analysis and analytical sub-domain prediction of mechanical torque.

flux linkage foreseen by FE analysis and analytical technique exhibits decent promise with $\sim 1\%$ error.

Tangential ($B_\theta$) and Radial ($B_r$) components of MFD in CPSFPMM are predicted under no-load and on-load conditions utilizing analytical sub-domain at the mid of air-gap. No load radial and tangential MFD components predicted by analytical sub-domain and existing FE analysis are shown in Figure. 7 and Figure. 8 respectively whereas on-load radial and tangential MFD components predicted by analytical sub-domain and existing FE analysis are shown in Figure. 9 and Figure. 10 respectively. Analysis reveals that predicted analytical sub-domain modelling under no load and on-load conditions fairly match with globally accepted FEA with peak relative error of $\sim 2\%$. Moreover, magnitude of the MFD components for the proposed design are higher when compare with the conventional design due to improved modulation effect which result better electromagnetic performances.

As shown in Figure. 11, cogging torque in CPSFPMM using MST is computed and compared with FEA using no load radial and tangential MFD components. According to study, the cogging torque predicted analytically for the CPSFPMM's original design exhibits immensely durable agreement with FE analysis, with $\sim 1.98\%$ error.

Finally, under loaded condition, mechanical torque is calculated in CPSFPMM using MST and compared with FEA using on-load radial and tangential MFD components as illustrated in Figure. 12. According to study, mechanical torque sub-domain modelling projected analytically for the CPSFPMM's original design exhibits extremely strong agreement with FE analysis, with $\sim 1.76\%$ error.

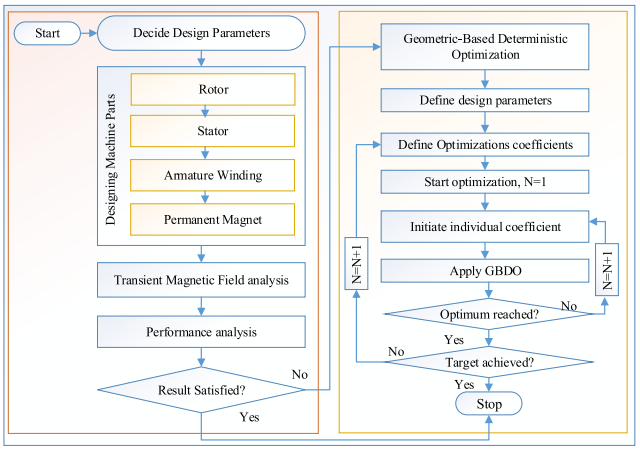


**FIGURE 13.** Flow of GBDO approach.

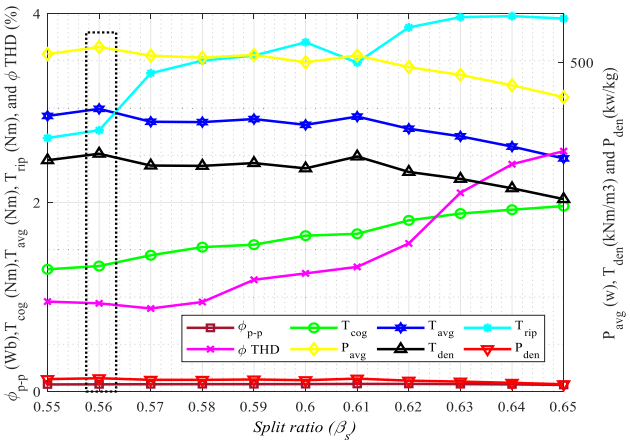


**FIGURE 14.** Influence of electromagnetic performances with $\beta_s$.

## VI. GEOMETRIC-BASED DETERMINISTIC OPTIMIZATION

GBDO is opted for improving performances of CPSFPMM with key performance pointer i.e., peak to peak open-circuit phase flux linkage ($\Phi_{p-p}$), peak to peak cogging torque ($T_{cog}$), average mechanical torque ($T_{avg}$), torque ripples ($T_{rip}$), open-circuit phase flux linkage Total Harmonic Distortion (THD) ($\Phi_{THD}$), average power ($P_{avg}$), torque density ($T_{den}$) and power density ($P_{den}$).

GBDO is opted in iteration with the overall flow as shown in the flow chart of Fig. 13. First an initial design is developed and to implement GBDO, different design parameters are selected based on their sensitivity such that design parameter with most sensitive should be followed first and then procced to another parameter with the optimum point of previous stage. GBDO consecutively optimize rotor and stator one-after-another and in sequence. Optimization goals are defined with main constraints as

$$\begin{cases} \textit{Objective function} \\ \max\left(T_{avg}, T_{den}, P_{avg}, P_{den}\right) \quad \textit{and} \\ \min\left(T_{cog}, T_{rip}, \Phi_{THD}\right) \end{cases} \tag{40}$$

$$\begin{cases} \textit{Constraint} \\ T_{avg} > 3Nm,\ \Phi_{p-p} > 0.80Wb,\ \Phi_{THD} < 2\% \\ T_{cog}, T_{rip} < 2Nm,\ T_{den} > 400kNm\Big/m^3 \\ \text{and} P_{den} > 50kNm\Big/m^3 \end{cases} \tag{41}$$

In order to ensure that the GBDO is applied solely to the design parameters and its configuration, it is important to note that the electrical loading (number of turns and applied current), magnetic loading (PM volume), axial length, slot area, and air gap length are all kept constant during implementation. Different design parameters selected for optimization are split ratio, rotor pole ratio, PM width, Flux bridge height, Flux bridge width, Slot depth, PM opening and stator yoke width. Note that the rotor pole optimization is carried out on rotor tip width and rotor base width for optimal rotor pole and it's respective shape.

In order to implement GBDO on aforesaid design parameters following optimization coefficients are specified

$$Split\ ratio = \beta_s = \frac{R_{os}}{R_{si}} \tag{42}$$

$$Rotor\ pole\ ratio = K_{rpr} = \frac{R_{rtw}}{R_{stw}} \tag{43}$$

$$PM\ width = K_{PMw} = \frac{W_{PM}}{\tau_s} \tag{44}$$

$$Flux\ barrier\ height = K_{fbh} = \frac{New\ R_{FBH}}{OrignalR_{FBH}} \tag{45}$$

$$Flux\ bridge\ width = K_{fbw} = \frac{New\ W_{FB}}{OrignalW_{FB}} \tag{46}$$

$$Stator\ yoke\ width = K_{syw} = \frac{Newh_{si}}{orignal\ h_{si}} \tag{47}$$

$$Rotor\ Slot\ depth = K_{rsd} = \frac{R_{rth}}{R_{rth} + R_{bi}} \tag{48}$$

$$PMo\ pening = K_{PMo} = \frac{New\ W_{PM}}{orignalW_{PM}} \tag{49}$$

Note that the order of optimization is same as the optimization coefficient is defined and the rotor pole ratio is separately applied to rotor tip ($K_{rpr\_tip}$) and base ($K_{rpr\_base}$). Moreover, quantitative electromagnetic performances and it's influence are discussed based on optimization coefficient as follow.

### A. INFLUENCE OF SPLIT RATIO

Split ratio is defined as the ratio of stator inner diameter to the stator outer diameter. This step helps to observe effects of stator and rotor back iron height. Due to magnetic saturation of stator yoke, maximum value of split ratio is restricted by $h_{si}/2$ and minimum is restricted to $2 * h_{si}$ to confirm uniform magnetic field distribution in stator tooth. Split ratio is very important design parameter which is utilized to achieve higher average mechanical torque. Electromagnetic performance analysis for different split ratio is shown in Figure. 14 which elaborate that split ratio is much sensitive to average

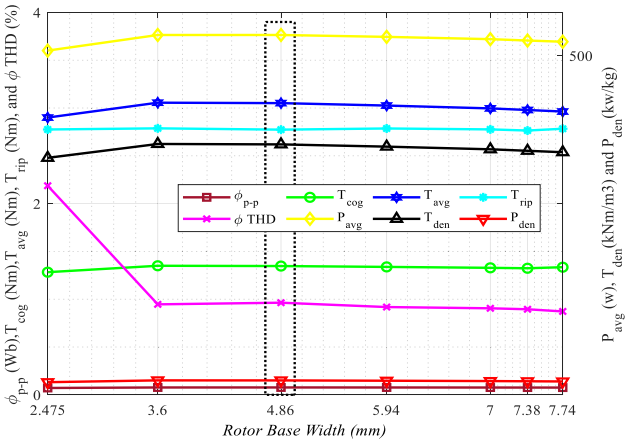


**FIGURE 15.** Electromagnetic performance with different rotor base width.

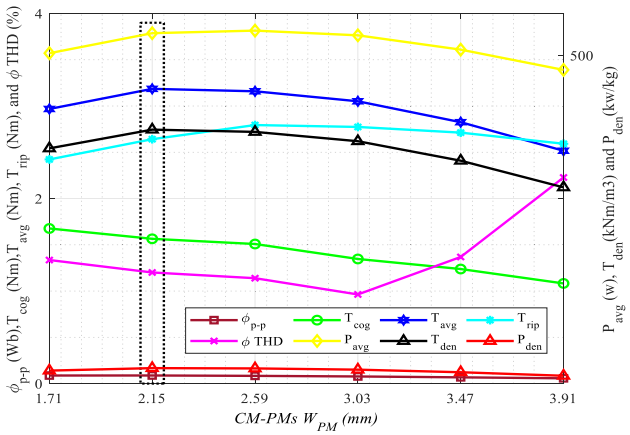


**FIGURE 16.** Illustration of electromagnetic performance with CM-PMs $W_{PM}$.

mechanical torque. It is notable that during split ratio optimization electric/magnetic loading, rotor pole width and stator pole width remains same. During this step, only rotor back iron height, stator yoke width and height of the flux bridge vary.

Initially, split ratio is 0.61 but electromagnetic performance analysis for split ratio shows that optimal split ratio obtained is 0.56 (shown by encircle) in which average mechanical torque is improved from 2.90 Nm to 2.99 Nm. Moreover, peak to peak cogging torque is reduces from 1.66 Nm to 1.32 Nm, no load open circuit phase flux THD from 1.31% to 0.91 % and torque ripples are reduced from 3.48 Nm to 2.76 Nm whereas torque density and power density are improved to 369.7 $kNm/m^3$ and 48.96 $kw/kg$ respectively. Therefore, the design with $\beta_s$=0.56 is selected for further optimization stages.

### B. INFLUENCE OF ROTOR BASE WIDTH

The ratio "$K_{rpr\_base}$" is varied for optimal selection of the rotor base width. Initially the base width is 7 mm which is varied in the range of 2.47 mm to 7.74 mm. Variation of electromagnetic performance for different rotor base width is shown in Figure. 15. It can be clearly seen that, at this stage the rotor base width has slight influence on electromagnetic performance. Therefore, the rotor base width will be optimized again with the rotor tip after stator optimization in the second cycle. Based on electromagnetic performance comparison, design with 4.86 mm rotor base width shows comparatively better results and selected for forgoing stator optimization.

### C. INFLUENCE OF CM-PMS WIDTH

This section investigates CM-PMs width dedicated optimization coefficient of $K_{PMw}$. The coefficient is evaluated in such a way that CM-PMs $W_{PM}$ are extended in the range of 1.71to 3.91 mm for optimal width which ensure least possible slotting effects. At this stage of optimization, the overall PM volume is kept constant by changing the RM-PMs spans above the h-shape tooth. The width of the adjoining flux barriers is adjusted together with the width change in the CM-PMs. Figure 16. shows the performance assessment for various CM-PM widths.

Performance evaluation discloses that CM-PMs $W_{PM}$ not only improve average mechanical torque from 3.05 Nm to 3.18 Nm but also strongly enhance open circuit phase flux linkage from 0.076 Wb to 0.087 Wb due to reduction in interaction between slots and PMs. Moreover, the increase in the average torque results higher torque density of 393.68 $kNm/m^3$, average power of 528.73 watt and power density of 52.14 $kw/kg$. Based on quantitative electromagnetic performance analysis, CPSFPMM having CM-PMs $W_{PM}$=2.15$mm$ for the foregoing optimization. Note that the initial CM-PMs $W_{PM}$ was 3.03 $mm$.

### D. INFLUENCE OF FLUX BARRIER HEIGHT

The partitioned PMs (RM-PMs and CM-PMs) used in the CPSFPMM are housed in a stator with an h-shaped design that includes a flux barriers and bridge. While flux barriers serve as the PM pole since the employed PMs are uni-polar whereas flux bridges offer an alternative magnetic channel to flux distribution to boost flux modulation.

In this section, electromagnetic performance is investigated with the height of the flux barrier as shown in Figure.17. Since the height of the flux bridge and barrier are same, only one of their heights needs to be developed, cutting down on computing time and further optimization processes.

During initial design, height of the flux barrier was set to be 37 mm which was later changed to 35.2 mm in split ratio optimization. During this optimization stage, the height of flux barrier is varied between 33.2 mm to 37.2 mm with the difference of 1 mm. In varying flux barrier height, overall magnet usage is kept constant by adjusting it through the RM-PMs span. Moreover, width of the flux bridge, width of the flux barrier, stator tooth, stator yoke, rotor pole, electrical loading, air gap and stack length remain unchanged.

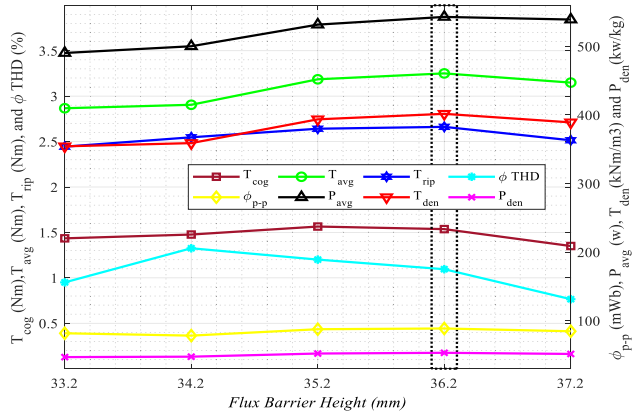


**FIGURE 17.** Electromagnetic performances analysis with varying flux barrier height.

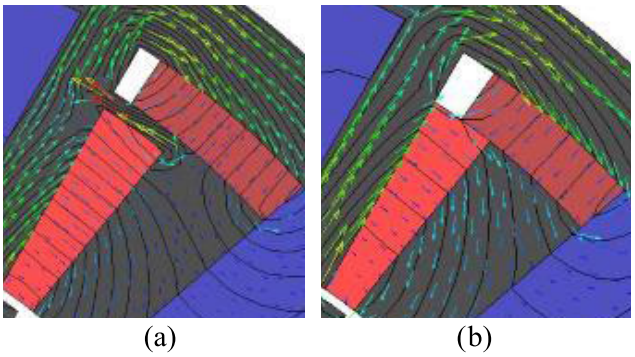


**FIGURE 18.** Flux cancellation and circulation in stator (a) with flux bridge (b) without flux bridge.

Detailed electromagnetic performances analysis as shown in Figure. 17 reveals that flux barrier is sensitive to open circuit phase flux linkage and average mechanical torque which leads to higher torque density. At optimal flux barrier height ($R_{FBH} = 36.2$ mm) the open circuit phase flux linkage increased from 0.087 Wb to 0.088 Wb and average mechanical torque from 3.18 Nm to 3.25 Nm. Moreover, in this step cogging torque is diminished by 5%, torque ripples are truncated by 4.8%, $\Phi_{THD}$ is reduced by 11.8%. In additional, the torque density and power density are enhanced to 401.69 $kNm/m^3$, and 53.20 $kw/kg$ respectively.

### E. INFLUENCE OF FLUX BRIDGE WIDTH

In design of CPSFPMM, partitioned PMs such RM/CM-PMs are physically segregated via flux bridge, which offers an additional channel to working harmonics for enhancing flux modulation. But, as seen in Figure 18, there is a major problem with leaky flux and flux cancellation because of the circulation of flux in the h-form stator tooth via stator yoke, flux bridge, and RM-PMs as display in Figure. 18(a). Therefore, flux bridge width is examined to achieve the least amount of flux circulation.

At prevent stress and saturation, $W_{FB}$ was initially fixed to 1 mm throughout the design process. W FB varies between

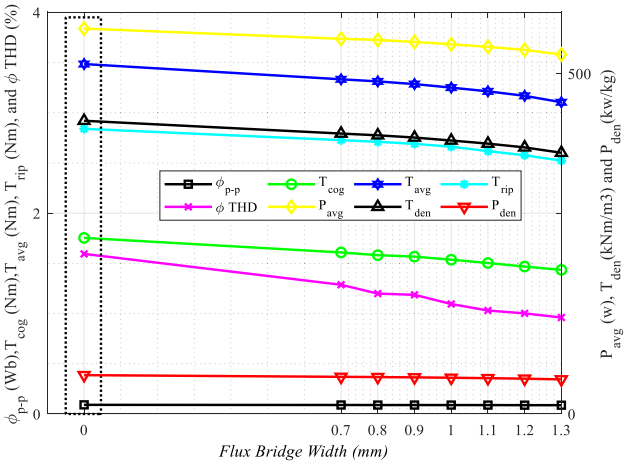


**FIGURE 19.** Influence of flux bridge width on electromagnetic performances CPSFPMM.

0.7 mm and 1.3 mm during GBDO. Figure. 19 detailed electromagnetic examination demonstrates that electromagnetic performance significantly improves at lower $W_{FB}$ but that a narrow flux bridge is put under stress. The flux bridge is therefore removed in order to address the saturation and stress problems on thin flux bridge.

Quantitative electromagnetic analysis at $W_{FB} = 0$ $mm$ in Figure. 19 shows that open circuit phase flux linkage is improved to 0.09 Wb from 0.088 Wb due to decrease in circulating and cancellation flux at the h-shaped portion as shown in Figure. 18(b). Due to significant compensation of cancellation flux, the average mechanical torque is boost to 3.48 Nm from 3.25 Nm which leads to higher torque density of 430.72 $kNm/m^3$. Moreover, average power and power density are enhanced to 566.16 watt and 57.07 $kw/kg$ respectively. However, cogging torque and torque ripples slightly increases but still within the desired target range.

### F. INFLUENCE OF ROTOR POLE

The rotor pole is optimized in two separate steps. First the rotor base width is optimized and then proceed to the rotor tip width. Both these steps effectively optimized the rotor pole to improve open circuit phase flux linkage without interfering average mechanical torque.

Initially, the rotor base width is 4.68 mm and rotor tip width 3.6 mm. The rotor base width is varied between 3.6 mm to 6 mm whereas rotor tip width is varied between 3 mm and 4.8 mm at the difference of 0.2 mm.

Comprehensive performance with changing rotor base width and rotor tip width as display in Figure. 20 and Figure. 21 respectively. Analysis reveals that at both rotor base and rotor tip width optimization, the average electromagnetic slightly increased and open circuit phase flux linkage is boost up to 0.091 Wb and 0.093 Wb at optimal rotor base width and rotor tip width respectively. The optimal rotor base width and rotor tip width are selected

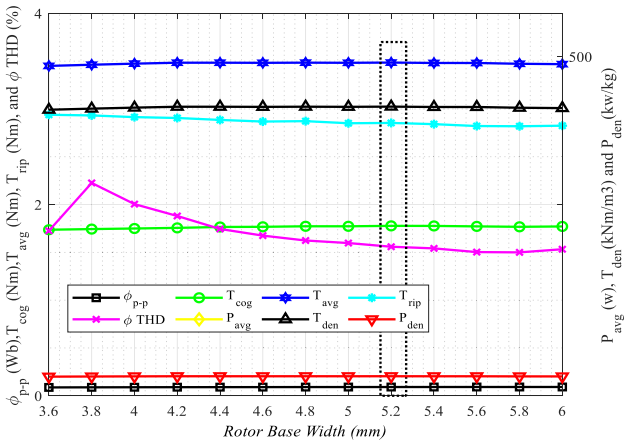


**FIGURE 20.** Electromagnetic performance analysis with different rotor base width.

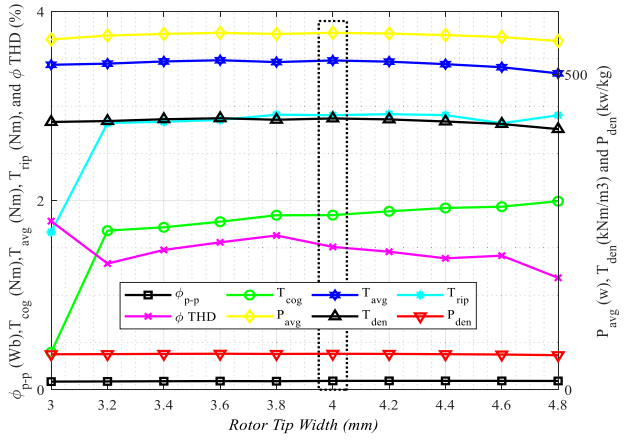


**FIGURE 21.** Investigation of electromagnetic performance at different rotor tip width.

as 5.2 mm and 4 mm respectively. The phenomena of increase in phase flux linkage is illustrate with the help of Figure 22.

Figure. 22 illustrate how the open circuit phase flux linkage boost with the rotor pole optimization. For a 3-phase, 13-rotor poles and 12-stator slots, Maximum open-circuit phase flux linkages have been seen to occur when the rotor poles and stator slot are positioned such that they face each other in the middle at the d-axis. Figure. 22(a) demonstrates that the left edge of the original rotor pole is not entirely aligned with the stator tooth (flux barrier) at the same mechanical degree, ensuing lesser phase flux linkage. A larger percentage of rotor poles aligning with the stator teeth at the same mechanical degree would increase the phase flux linkage. This is done with the help of rotor pole optimization where rotor tip is varied at the same mechanical degree. The phase flux linkage is increased with the wider rotor pole and can be clearly seen from Figure. 22(b) that the rotor pole is fully aligned to stator tooth.

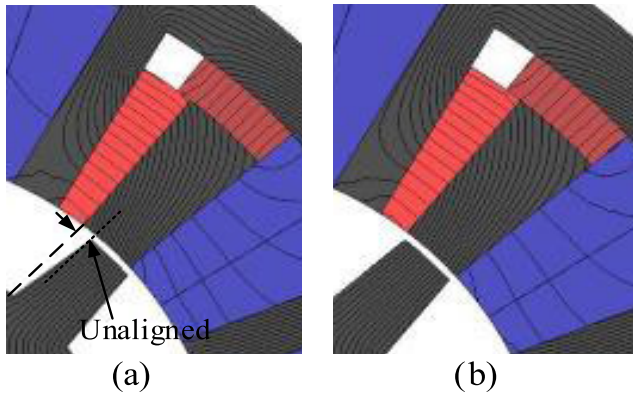


**FIGURE 22.** Optimal rotor pole width for maximum open circuit phase flux linkage (a) Original rotor pole unaligned with stator tooth (b) Optimized rotor pole aligned with stator tooth.

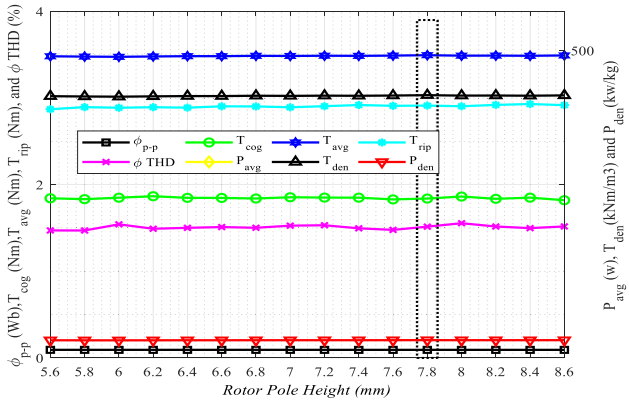


**FIGURE 23.** Electromagnetic analysis of key performance indicators at different rotor pole height.

### G. INFLUENCE OF ROTOR POLE HEIGHT

CPSFPMM is double salient rotor structure made of iron only. The operating principle clarifies that mechanical torque is produced due to partitioned CM/RM PMs. The magnetic flux produced by partitioned PM flow through air gap in the rotor and stator.

The influence of rotor pole height on electromagnetic performance is investigate in the range of 5.6 mm to 8.6 mm. Initially, the rotor pole height was set to be 6.6 mm however, performance analysis utilizing GBDO at different rotor pole as seen in Figure. 23 shows that higher mechanical torque and open-circuit phase flux linkage can be achieved when the rotor pole height is greater or equal to two times of the stator tooth. It is also confirmed from analysis that the optimal rotor pole height is selected to be 7.8 mm as encircled by dotted line. In this step, the average mechanical torque reaches to 3.49 Nm and the phase flux linkage to 0.0935 Wb whereas cogging torque, torque ripple, $\Phi_{THD}$, average power, torque density and power density almost remain the same.

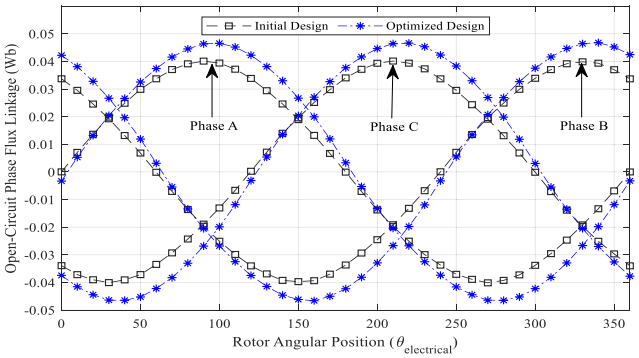


**FIGURE 24.** Comparison of no-load open-circuit phase flux linkage of initial and optimized designed.

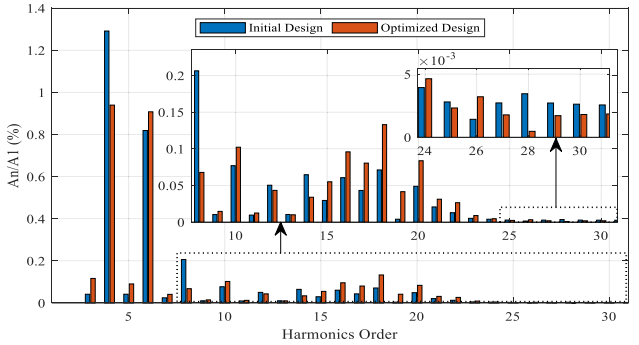


**FIGURE 25.** Comparison of no-load open-circuit phase flux linkage harmonics distribution for initial and optimized designed.

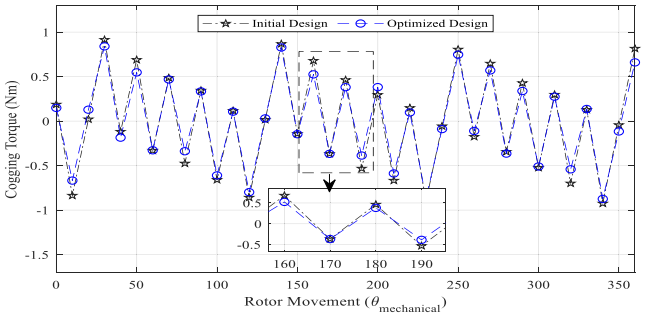


**FIGURE 26.** Cogging torque comparison between initial and optimized designed.

## VII. PERFORMANCE COMPARISON

Electromagnetic performance with metric encompassing graphical and tabulated quantitative analysis before and after GBDO is carried out in this section to validate and investigate electromagnetic performance of initial and optimized design as well as compare with conventional design. Key performance indicators of initial optimize design such as 3-phase no-load open-circuit phase flux linkage is shown in Figure. 24 with corresponding harmonics in Figure.25 whereas cogging torque and instantaneous mechanical torque are shown in Figure. 26 and Figure. 27 respectively.

Detail electromagnetic study of initial, optimized, and conventional designs are listed in table 2. Moreover,

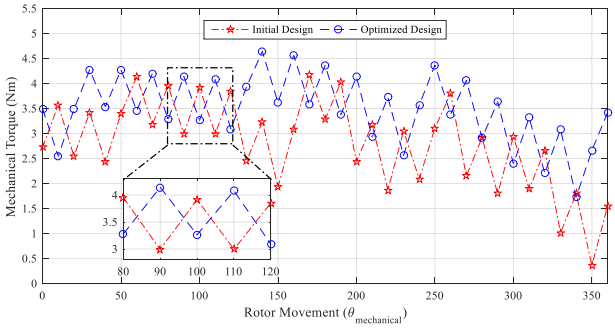


**FIGURE 27.** Instantaneous mechanical torque comparison between initial and optimized designed.

**TABLE 2.** Quantitative electromagnetic performance evaluation before and after GBDO with conventional design.

| Key performance indicators | Initial design | Optimized design | Conventional design |
|---|---|---|---|
| $\Phi_{p-p}$ $(wb)$ | 0.080527 | 0.093134 | 0.101213 |
| $T_{cog}$ $(Nm)$ | 1.839501 | 1.669271 | 2.555214 |
| $T_{avg}$ $(Nm)$ | 2.909393 | 3.494062 | 3.809913 |
| $T_{rip}$ $(Nm)$ | 3.480672 | 2.912506 | 3.653006 |
| $\Phi_{THD}$ (%) | 1.515024 | 1.318971 | 1.822143 |
| $T_{den}$ $(kNm/m^3)$ | 365.7523 | 431.83219 | 321.3353 |
| $P_{den}(kw/kg)$ | 48.44402 | 57.196317 | 42.56097 |
| $V_{PM}(mm^3)$ | | 10505.75 | 11856.55 |
| *PM cost ($)* | | 11.81 | 13.33 |

**TABLE 3.** Design parameters before and after optimization.

| Parameter | Initial value | Optimized value |
|---|---|---|
| $\beta_s$ | 0.61 | 0.56 |
| $R_{sy}$ | 41.4 | 40 |
| $R_{FBH}$ | 37 | 36.2 |
| $h_{si}$ | 3.6 | 5 |
| $R_{si}$ | 27.5 | 25.2 |
| $R_{ri}$ | 20.4 | 16.9 |
| $R_{or}$ | 27 | 24.7 |
| $W_{PM}$ | 3.03 | 2.15 |
| $R_{rtw}$ | 3.6 | 4 |

a comprehensive comparison with different topologies of SFPMM are carried out in [28] and [29]. Analysis demonstrates that GBDO successfully achieved the targeted torque, higher torque density and open-circuit phase flux linkage without interfering other parameters. It can be clearly seen that, the peak-to-peak flux linkage is increased by 15.65%, peak to peak cogging torque is diminish by 9.25%, enhance average mechanical torque by 20.09%, supress torque ripples by 16.32%, truncate harmonics of phase flux linkage by 12.94%, raise average power by 11.22%, boost torque density and power density by 18.08% and 18.06% respectively.

In addition, proposed topology of CPSFPMM with reduced PM and without flux bridge is compared with the conventional CPSFPMM with flux bridge and more PM usage. It is worth mentioning that developed model utilizes 46.53% of

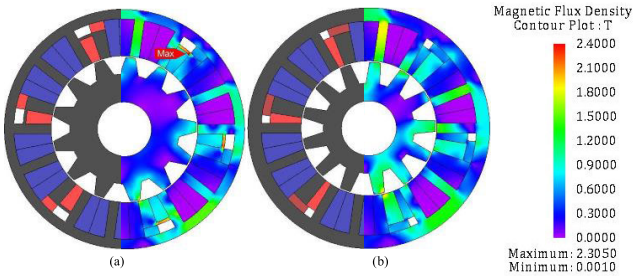


**FIGURE 28.** CPSFPMM view (a) Initial design (b) Optimized design.

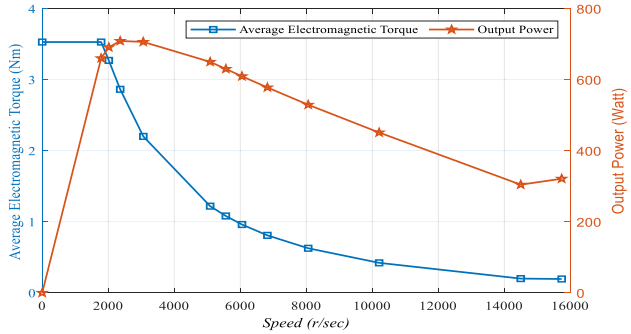


**FIGURE 29.** Optimized design torque and power vs speed curve.

the total PM volume. Despite of the reduced PM usage, the develop model successfully suppressed flux circulation and cancellation effect. Table. 2 offers a comprehensive performance illustration of proposed and conventional topology. Analysis reveals that proposed CPSFPMM without flux bridge reduces $T_{cog}$ by 34.90%, $T_{rip}$ by 20.27%, $\Phi_{THD}$ by 28.02% whereas it enhanced $P_{avg}$ by 17.79%, $T_{den}$ and $P_{den}$ by 34.38% at the cost of 8.67 % and 9.03% $\Phi_{p-p}$ and $T_{avg}$ respectively.

The initial and optimized design with Nephogram is shown in Figure. 28 and their respective parameters are listed in table 3. It can be clary seen from Figure. 28(a) that the flux bridge in the initial design saturate which degrade the electromagnetic performance. Therefore, the flux bridge in optimized design is eliminated during optimization process. The maximum magnetic flux density is 2.418 T at the saturation point of the flux bridge. Moreover, optimized design as shown in Figure 28(b) illustrate that no part of the machine saturates. Hence improve magnetic flux distribution and results better electromagnetic performance.

The torque and power vs speed curves in Figure. 29 demonstrate CPSFPMM design, which has been suggested to be used torque higher speed applications. Moreover, from Figure. 30, it can be clearly seen that when operating the proposed CPSFPMM under higher current densities and varying current phase, it is found that higher mechanical torque and lower torque ripples are achieved when d-axis current are set zero.

Furthermore, proposed CPSFPMM is validated by comparing it with various E/C-core SFPMM. Extensive

**TABLE 4.** Performance of various conventional E/C SFPMM.

| Key performance indicator (unit) | 12S-10P E-Core | 6S-10P E-Core | 6S-10P C-Core |
|---|---|---|---|
| $T_{avg}$ (Nm) | 2.25 | 3.83 | 3.2 |
| $T_{cog}$ (Nm) | 3.21 | 3.25 | 2.66 |
| $T_{rip}$ (Nm) | 3.87 | 3.23 | 2.54 |
| $T_{den}$ $(kNm/m^3)$ | 214.35 | 364.93 | 304.96 |
| $P_{den}$ $(kW/kg)$ | 28.39 | 48.33 | 40.39 |
| $V_{PM}(mm^3)$ | | 10505.75 | |
| $PM\ cost$ ($) | | 11.81 | |

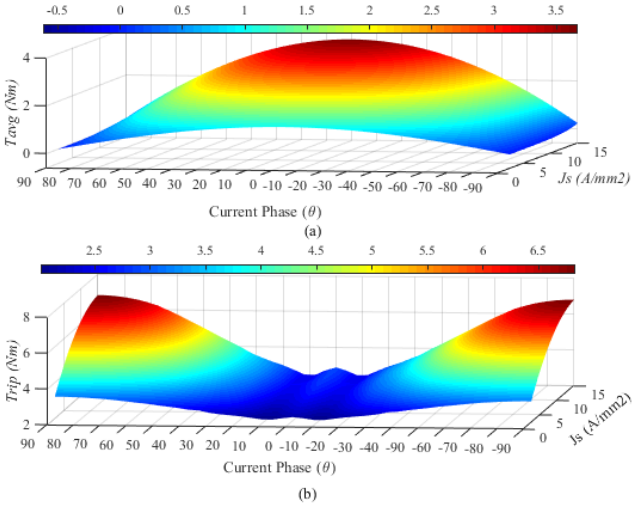


**FIGURE 30.** Investigation of torque characteristics with varying current density and applied current phase angle (a) $T_{avg}$ and (b) $T_{rip}$.

**TABLE 5.** 2D and 3D based electromagnetic performance.

| Key performance indicators | 2D FEA | 3D FEA |
|---|---|---|
| $\Phi_{p-p}$ $(wb)$ | 0.093 | 0.092 |
| $T_{cog}$ $(Nm)$ | 1.669 | 1.641 |
| $T_{avg}$ $(Nm)$ | 3.494 | 3.485 |
| $T_{rip}$ $(Nm)$ | 2.912 | 2.907 |
| $\Phi_{THD}$ (%) | 1.318 | 1.303 |
| $T_{den}$ $(kNm/m^3)$ | 431.832 | 431.825 |
| $P_{den}(kw/kg)$ | 57.196 | 57.185 |

electromagnetic performance analysis is in table 4. Finally, result is evaluated with 3D FEA utilizing JMAG FEA package. Performance of 2D and 3D FEA are recorded in table 5 for comparison.

## VIII. CONCLUSION

In this paper, a novel CPSFPMM design with partitioned PM and a flux barrier is developed, which improves the effects of flux modulation and lowers the overall PM volume by 46.53%. According to FE analysis, removing flux bridges, which impeded flux cancellation and circulation and offered a different track via flux barriers, improved modulation. Additionally, analytical model is used in the initial design and verified using the widely used FEA tool JMAG designer v. 18.1. Performance i.e.,$T_{cog}$, $T_{rip}$, $\Phi_{THD}$, $P_{avg}$, $T_{den}$

and $P_{den}$ are refined utilizing GBDO. FE analysis reveals that proposed CPSFPMM topology reduces $T_{cog}$ by 34.90%, $T_{rip}$ by 20.27%, $\Phi_{THD}$ by 28.02% whereas it enhanced $P_{avg}$ by 17.79%, $T_{den}$ and $P_{den}$ by 34.38%. As a result, the authors are satisfied in their decision to use an analytical approach for the initial sizing and GBDO for improving performances.

## REFERENCES

[1] N. Ullah, F. Khan, W. Ullah, A. Basit, M. Umair, and Z. Khattak, "Analytical modelling of open-circuit flux linkage, cogging torque and electromagnetic torque for design of switched flux permanent magnet machine," *J. Magn.*, vol. 23, no. 2, pp. 253–266, Jun. 2018.

[2] N. Ullah, F. Khan, W. Ullah, M. Umair, and Z. Khattak, "Magnetic equivalent circuit models using global reluctance networks methodology for design of permanent magnet flux switching machine," in *Proc. 15th Int. Bhurban Conf. Appl. Sci. Technol. (IBCAST)*, Jan. 2018, pp. 397–404.

[3] Z. Q. Zhu, L. J. Wu, and Z. P. Xia, "An accurate subdomain model for magnetic field computation in slotted surface-mounted permanent magnet machines," *IEEE Trans. Magn.*, vol. 46, no. 4, pp. 1100–1115, Apr. 2010.

[4] L. I. Jusoh, E. Sulaiman, R. Kumar, and F. S. Bahrim, "Design and performance of 8Slot-12Pole permanent magnet flux switching machines for electric bicycle application," *Int. J. Power Electron. Drive Syst.*, vol. 8, no. 1, pp. 248–254, 2017.

[5] Z. Q. Zhu, Y. Pang, J. T. Chen, R. Owen, D. Howe, S. Iwasaki, R. Deodhar, and A. Pride, "Analysis and reduction of magnet eddy current loss in flux-switching PM machines," in *Proc. 4th IET Conf. Power Electron., Mach. Drives*, Apr. 2008, pp. 120–124.

[6] Z. Q. Zhu, "Switched flux permanent magnet machines—Innovation continues," in *Proc. Int. Conf. Electr. Mach. Syst.*, Aug. 2011, pp. 1–10.

[7] Z. Q. Zhu and J. Chen, "Advanced flux-switching permanent magnet brushless machines," *IEEE Trans. Magn.*, vol. 46, no. 6, pp. 1447–1453, May 2010.

[8] J. T. Chen, Z. Q. Zhu, S. Iwasaki, and R. P. Deodhar, "A novel E-core switched-flux PM brushless AC machine," *IEEE Trans. Ind. Appl.*, vol. 47, no. 3, pp. 1273–1282, May/Jun. 2011.

[9] R. Owen, Z. Q. Zhu, J. B. Wang, D. A. Stone, and I. Urquhart, "Mechanically adjusted variable-flux concept for switched-flux permanent-magnet machines," in *Proc. Int. Conf. Electr. Mach. Syst.*, Beijing, China, Aug. 2011, pp. 1–6.

[10] Z. Q. Zhu, M. M. J. Al-Ani, X. Liu, M. Hasegawa, A. Pride, and R. Deodhar, "Comparison of alternate mechanically adjusted variable flux switched flux permanent magnet machines," in *Proc. IEEE Energy Convers. Congr. Expo. (ECCE)*, Raleigh, NC, USA, Sep. 2012, pp. 3655–3662.

[11] Y. Du, C. Zhang, X. Zhu, F. Xiao, Y. Sun, Y. Zuo, and L. Quan, "Principle and analysis of doubly salient PM motor with ⊓-shaped stator iron core segments," *IEEE Trans. Ind. Electron.*, vol. 66, no. 3, pp. 1962–1972, Mar. 2019.

[12] G. Zhao and W. Hua, "Comparative study between a novel multi-tooth and a V-shaped flux-switching permanent magnet machines," *IEEE Trans. Magn.*, vol. 55, no. 7, pp. 1–8, Jul. 2019.

[13] G. Zhao and W. Hua, "A novel flux-switching permanent magnet machine with v-shaped magnets," *AIP Adv.*, vol. 7, no. 5, Feb. 2017, Art. no. 056655.

[14] L. Zhang, L. J. Wu, X. Huang, Y. Fang, and Q. Lu, "A novel structure of doubly salient permanent magnet machine in square envelope," *IEEE Trans. Magn.*, vol. 55, no. 6, pp. 1–5, Jun. 2019.

[15] J. Li, K. Wang, F. Li, S. S. Zhu, and C. Liu, "Elimination of even-order harmonics and unipolar leakage flux in consequent-pole PM machines by employing N-S-iron–S-N-iron rotor," *IEEE Trans. Ind. Electron.*, vol. 66, no. 3, pp. 1736–1747, Mar. 2019.

[16] J. Li, K. Wang, and C. Liu, "Comparative study of consequent-pole and hybrid-pole permanent magnet machines," *IEEE Trans. Energy Convers.*, vol. 34, no. 2, pp. 701–711, Jun. 2019.

[17] F. Li, K. Wang, H. Sun, and J. Kong, "Influence of various magnetic pole on electromagnetic performance of consequent-pole permanent magnet machine," *IEEE Access*, vol. 7, pp. 121853–121862, 2019.

[18] J. Li and K. Wang, "A novel spoke-type PM machine employing asymmetric modular consequent-pole rotor," *IEEE/ASME Trans. Mechatronics*, vol. 24, no. 5, pp. 2182–2192, Oct. 2019.

[19] Y. Gao, D. Li, R. Qu, H. Fang, H. Ding, and L. Jing, "Analysis of a novel consequent-pole flux switching permanent magnet machine with flux bridges in stator core," *IEEE Trans. Energy Convers.*, vol. 33, no. 4, pp. 2153–2162, Dec. 2018.

[20] W. Ullah, F. Khan, E. Sulaiman, M. Umair, N. Ullah, and B. Khan, "Analytical validation of novel consequent pole E-core stator permanent magnet flux switching machine," *IET Electr. Power Appl.*, vol. 14, no. 5, pp. 789–796, 2020, doi: 10.1049/iet-epa.2019.0257.

[21] T. L. Tiang, D. Ishak, C. P. Lim, and M. K. M. Jamil, "A comprehensive analytical subdomain model and its field solutions for surface-mounted permanent magnet machines," *IEEE Trans. Magn.*, vol. 51, no. 4, pp. 1–14, Apr. 2015.

[22] J. Fu and C. Zhu, "Subdomain model for predicting magnetic field in slotted surface mounted permanent-magnet machines with rotor eccentricity," *IEEE Trans. Magn.*, vol. 48, no. 5, pp. 1906–1917, May 2012.

[23] B. L. J. Gysen, E. Ilhan, K. J. Meessen, J. J. H. Paulides, and E. A. Lomonova, "Modeling of flux switching permanent magnet machines with Fourier analysis," *IEEE Trans. Magn.*, vol. 46, no. 6, pp. 1499–1502, Jun. 2010.

[24] Y. Oner, Z. Q. Zhu, L. J. Wu, and X. Ge, "Analytical sub-domain model for predicting open-circuit field of permanent magnet Vernier machine accounting for tooth tips," *COMPEL, Int. J. Comput. Math. Electr. Electron. Eng.*, vol. 35, no. 2, pp. 624–640, Mar. 2016.

[25] L. J. Wu, Z. Q. Zhu, D. Staton, M. Popescu, and D. Hawkins, "Analytical modeling of eddy current loss in retaining sleeve of surface-mounted PM machines accounting for influence of slot opening," in *Proc. IEEE Int. Symp. Ind. Electron.*, Hangzhou, China, May 2012, pp. 611–616.

[26] Y. Oner, Z. Q. Zhu, L. J. Wu, X. Ge, H. L. Zhan, and J. T. Chen, "Analytical on-load subdomain field model of permanent-magnet Vernier machines," *IEEE Trans. Ind. Electron.*, vol. 63, no. 7, pp. 4105–4117, Jul. 2016.

[27] K. J. Binns, P. J. Lawrenson, and C. W. Trowbridge, *The Analytical and Numerical Solution of Electric and Magnetic Fields*. Hoboken, NJ, USA: Wiley, 1992.

[28] W. Ullah, F. Khan, N. Ullah, M. Umair, B. Khan, and H. A. Khan, "Comparative study between C-core/E-core SFPMM with consequent pole SFPMM," in *Proc. Int. Symp. Recent Adv. Electr. Eng. (RAEE)*, Islamabad, Pakistan, 2019, pp. 1–6.

[29] W. Ullah, F. Khan, and E. Sulaiman, "Sub-domain modelling and multivariable optimisation of partitioned PM consequent pole flux switching machines," *IET Electr. Power Appl.*, vol. 14, no. 8, pp. 1360–1369, Aug. 2020, doi: 10.1049/iet-epa.2019.0993.

[30] W. Ullah, F. Khan, E. Sulaiman, I. Sami, and J.-S. Ro, "Analytical subdomain model for magnetic field computation in segmented permanent magnet switched flux consequent pole machine," *IEEE Access*, vol. 9, pp. 3774–3783, 2021.

**WASIQ ULLAH** (Member, IEEE) was born in Peshawar, Khyber Pakhtunkhwa, Pakistan, in 1995. He received the B.S. and M.S. degrees in electrical (power) engineering from COMSATS University Islamabad (Abbottabad Campus), Abbottabad, Pakistan, in 2018 and 2020, respectively, where he is currently pursuing the Ph.D. degree in electrical (power) engineering.

Since 2018, he has been a Research Associate with the Electric Machine Design Research Laboratory. His research interests include analytical modeling, design analysis and optimization of permanent magnet flux switching machines, linear flux switching machines, hybrid excited flux switching machines, novel consequent pole flux switching machines for high-speed brushless AC applications, and flux switching generators for counter-rotating wind turbines applications.

Dr. Ullah is a member of IEEE-IES Electrical Machines Technical Committee and the Pakistan Engineering Council. He serve as a Reviewer for IEEE TRANSACTION ON MAGNETICS, IEEE ACCESS, *IET Journals*, *MDPI Journals*, IECON–2022, and 2022 IEEE Energy Conversion Congress and Exposition (ECCE 2022).

**FAISAL KHAN** (Senior Member, IEEE) was born in Charsadda, Khyber Pakhtunkhwa, Pakistan, in 1986. He received the B.S. degree in electronics engineering and the M.S. degree in electrical engineering from COMSATS University Islamabad (Abbottabad Campus), Pakistan, in 2009 and 2012, respectively, and the Ph.D. degree in electrical engineering from Universiti Tun Hussein Onn Malaysia, Malaysia, in 2017.

From 2010 to 2012, he was a Lecturer at the University of Engineering and Technology, Abbottabad, Pakistan. Since 2017, he has been an Assistant Professor with the Electrical and Computer Engineering Department, COMSATS University Islamabad (Abbottabad Campus). He is the author of more than 100 publications and one patent. His research interests include design and analysis of flux-switching machines, synchronous machines, and DC machines.

Dr. Khan is a member of IEEE-IES Electrical Machines Technical Committee and the Pakistan Engineering Council. He has received a multiple research awards.

**SHAHID HUSSAIN** (Graduate Student Member, IEEE) was born in Swabi, KPK, Pakistan. He received the B.S. degree in electrical (power) engineering from COMSATS University Islamabad, Abbottabad Campus, Abbottabad, Pakistan, in 2019, where he is currently pursuing the M.S. degree in electrical (power) engineering. He has been a Research Assistant with the Electric Machine Design Research Laboratory, since 2020. His research interests include design analysis, optimization and experimental validation of modular and complementary fault tolerant field excited linear flux switching machines for long stroke application. He is a member of the Pakistan Engineering Council.

**MUHAMMAD YOUSAF** (Graduate Student Member, IEEE) received the B.S. degree in electrical engineering (electronics) from the Federal Urdu University of Arts Science and Technology (FUUAST), Islamabad, Pakistan, in 2015, and the M.S. degree in electrical engineering from COMSATS University Islamabad, Islamabad, in 2019, where he is currently pursuing the Ph.D. degree in electrical engineering. His research interests include design, analysis, and optimization of permanent magnet flux switching machines, multi-phase machines, and axial flux permanent magnet machines.

**SIDDIQUE AKBAR** was born in KPK, Pakistan, in 1997. He received the bachelor's degree in electrical (power) engineering from COMSATS University Islamabad, Abbottabad Campus, Pakistan, in 2020, where he is currently pursuing the M.S. degree in electrical engineering. He has been a Research Assistant at the Electric Machine Design Research Laboratory, since 2020. His research interests include analysis, optimization, and experimental validation of actuator and flux switching machines.